

## **Progress this week**

**March 29, 2020**

- Added an abstract.
- Added some example LGCP applications to 1.1.
- Rearranged 2 to clarify SPDE vs Simpson.
- Added the rest of the math and notation to 2 and 3.
- Added an explanation of the prior specification in 3.1.1 and refit the models with priors that better illustrate the prior selection choices.
- Added citations throughout.

**Previous word count:** 6872  
**Previous page count:** 21

**Current word count:** 7406  
**Current page count:** 22.5

## REVIEW ARTICLE

# The Integrated Nested Laplace Approximation applied to Spatial Log-Gaussian Cox Process Models

Kenneth Flagg and Andrew Hoegh

Montana State University, Bozeman, MT

### ARTICLE HISTORY

Compiled March 24, 2020

### ABSTRACT

Spatial point process models are theoretically useful for mapping discrete events, such as plant or animal presence, across space. The computational complexity of fitting these models is often a barrier to their practical use. The log-Gaussian Cox process (LGCP) is a point process driven by a latent Gaussian field, and recent advances have made it practical to fit Bayesian LGCP models using the integrated nested Laplace approximation (INLA). These advances include the stochastic partial differential equations (SPDE) approach to sparsely approximate the Gaussian field and an extension using pseudodata with a Poisson response. To help link the theoretical results to statistical practice, we provide an overview of these methods and then illustrate their implementation using freely available data. The examples include both a censused dataset and an incomplete data situation, and our well-commented R code is shared in the online supplement. Our intent is to make these methods accessible to the practitioner of spatial statistics without requiring deep knowledge of point process theory.

### KEYWORDS

Bayesian hierarchical model, INLA, spatial prediction, log-Gaussian Cox process, spatial point process

## 1. Introduction

Statistical methods for spatial prediction result in a high-dimensional inference problem that can present computational challenges, particularly for large datasets. For instance, when the goal of statistical modeling is to produce a graphical map of a random variable over space, the model ultimately must be able to predict that random variable at every pixel of the image. A map image will typically be at least several hundred by several hundred pixels, so in total there can easily be hundreds of thousands of pixels requiring predictions. Thus, even when a model has only half a dozen parameters, spatial prediction may require hundreds of thousands of latent variables.

Spatial point process models further complicate the situation; in addition to computational challenges due to a large number of latent variables and parameters, point process models also require evaluating difficult likelihoods. Both maximum likelihood and Bayesian model fitting require integrating the intensity function over space, but the integral is generally not available in closed form and, unlike a probability distribution, the integral over the entire domain does not necessarily equal one.

Many methods have been introduced for modeling spatial point patterns, including Poisson regression approximations, maximum pseudolikelihood, and Markov chain Monte Carlo [2, 3, 6, 24]. The number of parameters and latent variables in these models still poses a major computational challenge. This computational challenge led to the development of the integrated nested Laplace approximation (INLA).

INLA was introduced by Rue, Martino, and Chopin (2009), who sought fast and accurate posterior approximation for Bayesian additive regression models with Gaussian latent fields and allowing for non-Gaussian responses [28]. This setting includes random effects models, generalized linear models, spline models, dynamic models, spatial and spatiotemporal models, among others. A non-Gaussian response in one of these models typically results in the posterior having no closed form. The standard solution is MCMC due to ease of implementation and because the simulation error can always be made smaller by running the sampler for more iterations. However, INLA is much faster; Rue, Martino, and Chopin showed that INLA can find accurate and precise approximations in minutes or seconds when MCMC would take days or hours to achieve similar precision.

Development of INLA has made accurate approximate model fitting considerably more feasible for a particular class of log-Gaussian Cox process (LGCP) models. A key part of INLA’s computational simplicity is that it calculates the posterior distribution of each latent Gaussian variable one at a time; that is, it provides only the posterior marginal distributions rather than the full joint distribution.

When using a LGCP model for spatial mapping, two aspects make INLA a suitable approach. First, the LGCP is driven by a spatial Gaussian process (GP), so the latent variables are Gaussian. Second, even though the latent variables are expected to exhibit spatial dependence, their full joint distribution is not needed. In most situations it suffices to map their predicted values, variance, and upper and lower interval bounds pointwise across space.

We focus on spatial mapping using a hierarchical construction of the LGCP, and do so without discussing many classic spatial point process concepts such as Gibbs processes, Markov processes, point process densities, or the Papangelou conditional intensity function. For readers interested in the general spatial point process context in which the LGCP originates, we recommend other references [12, 13, 24].

Recently, there has been renewed interest in fitting LGCP models to incompletely-observed point patterns, known in the point process literature as variable sampling effort. This scenario arises when analysts seek to map the intensity across some domain, but cannot census every event in the domain. Instead, effort is made to observe events in certain sections of the domain. Either a subregion of the domain is sampled or a random subset of the events are sampled. The subregion situation commonly occurs when quadrat sampling is employed or when the domain is partitioned into areal regions and only certain regions can be surveyed. The random subset situation is best known from distance sampling, where a set of line transects are traversed and all events detected near the transects are recorded. The events are assumed to be detected with a probability depending on the distance from the transect. Hybrids of the subregion and random subset situation are possible when there is a hard limit to the distance at which events can be observed, for example because some equipment cannot leave the transect. Point patterns observed under variable sampling effort have traditionally been aggregated to the quadrat, transect, or grid cell level before analysis [13]. However, INLA aids the fitting of LGCP models to such data.

This article provides a review of recent advances in the fitting of spatial LGCP models via INLA, including a finite element approach for dimension reduction, a like-

likelihood factorization that avoids gridding, and incorporation of sampling effort or false negatives. The examples use a freely-available datasets and the R code is provided in the supplementary materials.

The remainder of Section 1 provides an overview of spatial LGCP models and INLA. Section 2 describes the methodology developed to fit LGCP models in INLA, and Section 3 presents example analyses of real-world data. Finally, Section 4 presents concluding remarks.

### 1.1. Log-Gaussian Cox Process

The log-Gaussian Cox process is a Poisson process driven by a latent Gaussian process [25]. This section provides a brief overview of the spatial Poisson process and then presents the hierarchical construction of the spatial LGCP.

A spatial point process generates a random set of events (points) in space. The process is characterized primarily by its intensity function  $\lambda(u)$ , which gives the local mean number of events per unit area at any point in space. The intensity function is nonnegative and defined on a domain  $\mathcal{D} \subset \mathbb{R}^2$ . The point process is observed in a bounded window  $\mathcal{R} \subset \mathcal{D}$ . The point process is denoted  $\mathbf{X}$ , and its realizations are  $\mathbf{x} = \{x_1, \dots, x_n\}$ . A realized (observed)  $\mathbf{x}$  is called a point pattern; the elements of the point pattern are the events.

The Poisson process is fully defined by its intensity function and satisfies the following two properties [24]:

- (1) The number of events in any region  $\mathcal{B}$  follows a Poisson distribution with mean  $\int_{\mathcal{B}} \lambda(u) du$ .
- (2) Given the number of events in  $\mathcal{B}$ , those events are independent and identically distributed with probability density  $\lambda(u) / \int_{\mathcal{B}} \lambda(u) du$ .

The distribution function of a Poisson process is

$$\pi(\mathbf{X}|\lambda) = \frac{\exp \left[ - \int_{\mathcal{R}} \lambda(u) du \right]}{n!} \prod_{x \in \mathbf{X}} \lambda(x)$$

as given in Cressie (1993) [12]. This can be extended to include further parameters used to define  $\lambda$ , most commonly coefficients to construct a log-linear model with covariates, or a polynomial or spline function of the spatial coordinates.

In a Poisson process, the intensity function is a fixed parameter (or a deterministic function of fixed parameters and covariates). In applications of spatial point process models, this is often too simplistic because spatial heterogeneity may be driven by other random processes with their own parameters about which inferences are desired.

A Cox process is a generalization of the Poisson process where the intensity function is a realization of another stochastic process [11, 13]. Conditional on the intensity function, a Cox process must satisfy the two Poisson process properties, but the intensity function can take any form. Cox processes are commonly used to model clustering of events, such as in the classic Neyman-Scott process where cluster centers are generated by another Poisson process [27]. Another example is where the intensity is a Dirichlet process mixture [32]. In situations where the intensity function is less structured but exhibits spatial autocorrelation, the Cox process can incorporate a geostatistical process. The log-Gaussian Cox process is an example of this.

The LGCP uses a log-linear model for the intensity

$$\log \lambda(u) = \Psi(u) = \mathbf{z}(u)' \boldsymbol{\beta} + \mathbf{e}(u),$$

where  $\mathbf{e}$  is a Gaussian process with mean 0 and covariance function  $C(u, v)$ .

Where the spatial Poisson process has a (stochastically) fixed intensity to be estimated from data, the spatial LGCP induces a hierarchical model where the intensity function is itself a random process to be predicted.

Spatial or spatiotemporal LGCP models have recently been applied to whale populations (Yuan et. al., 2017), landslides (Lombardo et. al., 2018), fMRI data (Samartsidis et. al., 2019), and disease mapping (Konstantinoudis et. al., 2020) to list only a few applications [18, 22, 29, 33]. Badeley et. al. (2005) and Möller and Waagepetersen (2007) present model checking tools for LGCP and other spatial point process models [5, 24].

## 1.2. Integrated Nested Laplace Approximation

INLA was developed with the goal of providing fast, accurate, deterministic approximations for posterior marginal distributions of the parameters in latent Gaussian models [28]. The setting is Bayesian generalized additive models but is kept very general; this includes linear models, models with nonlinear (spline, random walk, etc.) functions of predictors, and models with temporal and/or spatial dependence. Such models commonly include many Gaussian latent variables or parameters with Gaussian priors and relatively few non-Gaussian parameters. The INLA approach makes repeated use of Laplace expansion, numerical integration, and numerical search. The method has established usefulness for LGCP [17]. It is readily implemented using the standalone INLA software or in R via the R-INLA package [19].

Our objective in this section is to provide an overview of the mathematical motivation behind INLA while omitting technical details that can be found elsewhere. The notation used in this section is somewhat nonstandard, but consistent with spatial point process notation. Let  $\mathbf{y}$  be the response (vector). Let  $\boldsymbol{\xi}$  be a vector of all unobserved Gaussian variables in the model, including both parameters with Gaussian priors, and latent Gaussian variables such as random effects or values of a Gaussian field to be predicted. Let  $\boldsymbol{\theta}$  be a vector of all non-Gaussian model parameters. The posterior distribution is

$$\pi(\boldsymbol{\xi}, \boldsymbol{\theta} | \mathbf{y}) = \frac{\pi(\mathbf{y}, \boldsymbol{\xi}, \boldsymbol{\theta})}{\int \pi(\mathbf{y}, \boldsymbol{\xi}, \boldsymbol{\theta}) d\mathbf{y}},$$

but the integral is not available in closed form, so the posterior must be either sampled from or approximated. The INLA approach is to first find a Laplace approximation of  $\pi(\boldsymbol{\theta} | \mathbf{y})$ . Then, that result and a further Laplace expansion are used to approximate each posterior marginal  $\pi(\xi_i | \mathbf{y})$ , where  $\xi_i$  is the  $i$ th latent Gaussian variable in  $\boldsymbol{\xi}$ .

The derivation begins by invoking the definition of conditional probability, rewriting

$$\pi(\boldsymbol{\theta} | \mathbf{y}) \propto \frac{\pi(\mathbf{y}, \boldsymbol{\xi}, \boldsymbol{\theta})}{\pi(\boldsymbol{\xi} | \mathbf{y}, \boldsymbol{\theta})}.$$

The Laplace approximation is applied to the denominator, taking a second-order Taylor expansion of  $\log[\pi(\boldsymbol{\xi} | \mathbf{y}, \boldsymbol{\theta})]$  around the posterior mode of  $\boldsymbol{\xi}$  and then exponentiating. The result is a Gaussian approximation of  $\pi(\boldsymbol{\xi} | \mathbf{y}, \boldsymbol{\theta})$ . Then the approximate

posterior marginal distribution of  $\boldsymbol{\theta}$  is

$$\tilde{\pi}(\boldsymbol{\theta}|\mathbf{y}) \propto \frac{\pi(\mathbf{y}, \boldsymbol{\xi}, \boldsymbol{\theta})}{\pi_G(\boldsymbol{\xi}|\mathbf{y}, \boldsymbol{\theta})} \Big|_{\boldsymbol{\xi}=\boldsymbol{\xi}^*}$$

with  $\boldsymbol{\xi}^*$  denoting the posterior mode of  $\boldsymbol{\xi}$ .

A similar process is repeated for the posterior marginal of each  $\xi_i$ , beginning with

$$\pi(\xi_i|\mathbf{y}, \boldsymbol{\theta}) \propto \frac{\pi(\mathbf{y}, \boldsymbol{\xi}, \boldsymbol{\theta})}{\pi(\boldsymbol{\xi}_{-i}|\xi_i, \mathbf{y}, \boldsymbol{\theta})},$$

where the  $-i$  notation indicates that the  $i$ th element is omitted from the vector. The Laplace approximation of this denominator is still complicated, but further approximations make it tractable. The takeaway is that, by handling the Gaussian latent variables one at a time, computation can be made considerably simpler compared to methods that approximate the joint poster.

These approximations, as well as fast numerical integration methods and numerical optimization to find the posterior modes, are packaged in the INLA software and R-INLA library. The software offerings are stable and documented to the point that the applied statistician can use them without knowing all of the computational details.

## 2. Methodology

INLA provides an efficient computational framework for fitting Bayesian models with latent Gaussian variables. On top of this framework, several tools are built to further simplify the fitting of spatial LGCP models. The stochastic partial differential equation (SPDE) approach provides dimension reduction for the spatial GP [20]. The SPDE approach employs a numerical integration scheme which can also be used to approximate the LGCP likelihood and negate the need to grid the events into Poisson counts [30]. With these computational improvements, researchers are now able to efficiently fit LGCP models to large spatial point pattern datasets and even incompletely-observed point patterns [33].

### 2.1. The SPDE Approach

Because the LGCP includes a Gaussian process (GP), efficient computation for Gaussian processes is critical when working with LGCP models. The GP imposes a dense covariance matrix on the latent variables [7]. For GPs with a Matérn covariance function, a Gaussian Markov random field (GMRF) approximation can simplify computation, requiring only a sparse covariance structure.

The GMRF approximation is motivated by the fact that Gaussian fields with Matérn covariances are solutions to the stochastic partial differential equation (SPDE) below [20]:

$$\tau(\kappa^2 - \Delta)^{\alpha/2} \mathbf{e}(u) = \mathbf{W}(u), \quad u \in \mathbb{R}^d, \quad \kappa > 0, \quad \alpha = \nu + d/2, \quad \nu > 0.$$

Here,  $\mathbf{W}$  is a Gaussian white noise process with variance 1, and  $\Delta$  is the Laplacian operator. The stationary solution  $\mathbf{e}$  is a Gaussian field having a Matérn covariance

function with precision (inverse variance)  $\tau$ , scaling parameter  $\kappa$  (inversely proportional to the range effective), and smoothness parameter  $\nu$ .

Lindgren, Rue, and Lindström (2011) investigate the limit as  $\nu \rightarrow 0$  for  $d = 2$ , finding that the solution is a GMRF on a unit lattice [20]. They then construct approximations for positive integer values of  $\nu$  by  $\nu$ -fold convolution of  $\mathbf{e}$  with itself. Finally, they use a finite element method to generalize the approximation to arbitrary triangulations of the support. This approximation has considerable computational benefits because the GMRF has a sparse covariance structure; the only nodes with nonzero covariances are those directly connected by edges in the triangulation.

The core of the SPDE approach is the finite-element GMRF representation of the GP. The idea is to model the GP at the nodes (vertices) of a triangular mesh. Values at points other than the nodes are found by linear interpolation, resulting in a surface constructed from triangular faces. Figure 1 shows an example. The linear interpolation uses the barycentric coordinate system (Figure 2). The mathematical form of this interpolation is very simple; for a point  $u$  with barycentric coordinates  $(\alpha, \beta, \gamma)$  inside a triangle with vertices  $s_1, s_2, s_3$ , the approximation is simply

$$\mathbf{e}(u) \approx \alpha \mathbf{e}(s_1) + \beta \mathbf{e}(s_2) + \gamma \mathbf{e}(s_3).$$

This technique can approximate complicated surfaces as relatively low-dimensional vectors via a piecewise-linear approximation.

The full finite element representation is constructed in the following manner. Start with a triangular mesh over the spatial domain, with nodes  $s_1, \dots, s_m$ . Then define a set of basis functions  $\{\phi_1, \dots, \phi_m\}$  that map the spatial domain to the barycentric coordinate system. That is,  $\phi_i$  corresponds to node  $s_i$ , and for a point  $u$  there are at most three nonzero  $\phi_i(u)$ . The nonzero values give the barycentric coordinates of  $u$  in a triangle containing it. The finite element representation has the form

$$\mathbf{e}(u) \approx \sum_{j=1}^m \psi_j \phi_j(u).$$

The vector  $\boldsymbol{\psi} = (\psi_1, \dots, \psi_m)'$  is a realization of the GMRF, so it is a multivariate Gaussian vector comprised of the values of the latent field at the nodes.

The  $\psi_i$  values are used to compute averages and for numerical integration, in which cases they are weighted by the area represented by the nodes (Figure 3). The region represented by a node is called its dual region, denoted  $\text{dual}(s)$  for node  $s$ . The dual region is constructed by connecting the midpoints of the edges and centroids of the triangles for which the node is a vertex. The weight is the area of the dual region, which is one third of the total area of the triangles used in its construction.

In practice, the SPDE approach goes as follows. Choose nodes  $s_i$  at which to model  $\boldsymbol{\Psi}(s_i) = \mathbf{z}(s_i)'\boldsymbol{\beta} + \mathbf{e}(s_i)$ , then build a triangular mesh using these nodes. Typically the nodes will include locations where data or covariates are available, then the rest will be filled in with a Delaunay triangulation under some edge length constraints. The  $\mathbf{e}(s_i)$  are modeled as a GMRF where the distribution of each  $\mathbf{e}(s_i)$  depends only on the  $\mathbf{e}(s_j)$  where  $s_i$  and  $s_j$  are connected by an edge. The GMRF representation is assumed to be a piecewise linear approximation of the continuous Gaussian field;

The SPDE approach is implemented in the INLA package alongside tools for constructing meshes. A wrapper for easily specifying LGCP models is provided in the `inlabru` package [1].

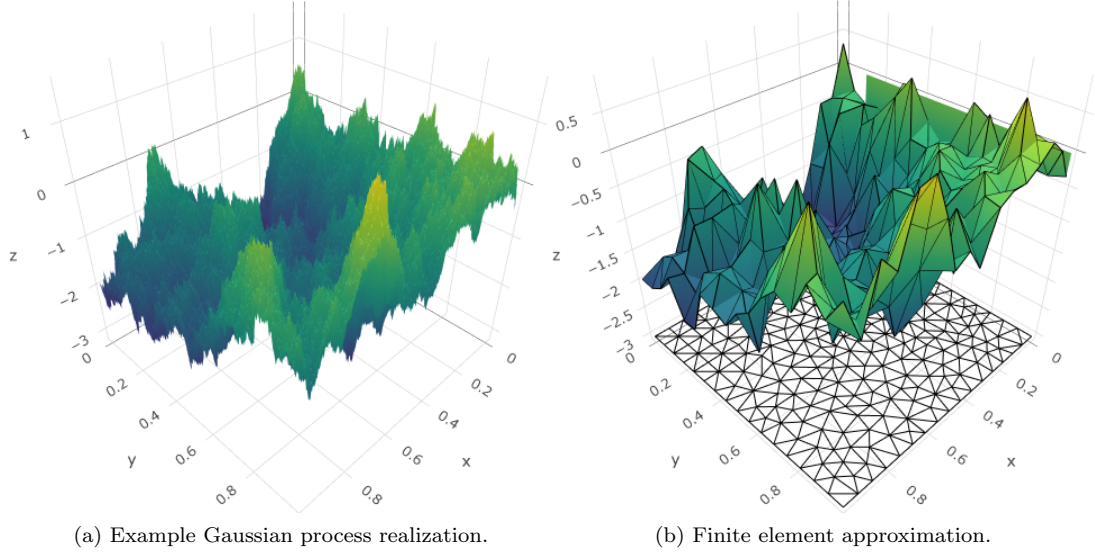


**Figure 1.** A realization of a spatial Gaussian process and an approximation of that realization over a triangular mesh.

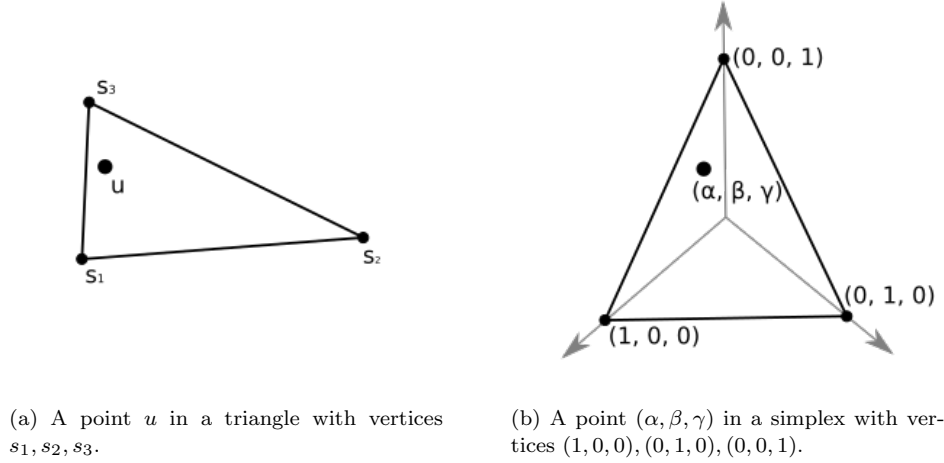


**Figure 2.** An illustration of the linear transformation from a mesh triangle to the 2-simplex. The transformation is defined from  $\mathbb{R}^2$  to  $\mathbb{R}^3$  such that the vertices are mapped to a unit vector along each axis. This transformation takes the point  $u$  to  $(\alpha, \beta, \gamma)$ , its barycentric coordinates. The barycentric coordinates have the property that  $\alpha + \beta + \gamma = 1$ .



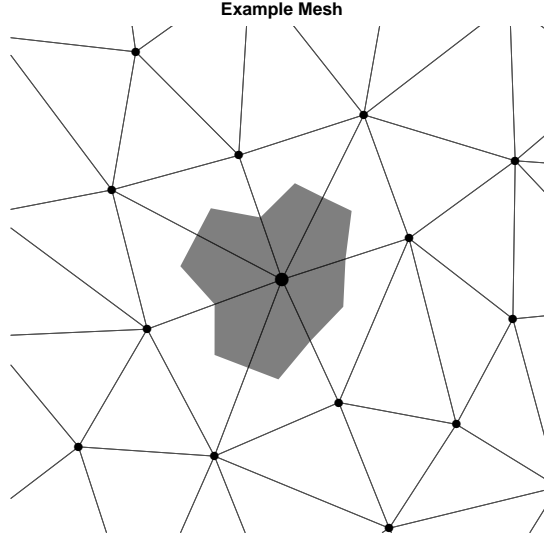


**Figure 3.** An illustration of the nodes (dots) and the weighting scheme for one node (large dot). In the SPDE approach, this node represents its dual region (shaded), so its weight is proportional to the shaded area. The dual region is constructed by connecting the midpoints of the node's edges to the midpoints of the adjacent triangles.

## 2.2. Going Off the Grid

Point pattern data are sometimes known as presence-only data, underscoring the fact that information about where events did *not* occur is both important and often overlooked. There have been many proposed methods to account for regions that were observed to contain no events (in contrast to unobserved regions where it is unknown if any events are present). Many of these methods involve imputation of dummy points or discretization. In the world of maximum likelihood, perhaps the most well-developed of these use approximations based on Poisson regression on presence/absence information in small disjoint regions [3, 6].

Another alternative, which is probably the most popular approach to Bayesian fitting of LGCP models but is also common in frequentist analyses, is to grid the domain and model the induced Poisson counts. It has long been understood that results are sensitive to the discretization scheme [8]. Simpson et. al. (2016) explain that this is also computationally wasteful [30].

Simpson et. al. took LGCP inference “off grid” by introducing a computationally-efficient approximation to the Poisson process likelihood that requires the intensity function only to be evaluated at the locations of observed events and at the nodes of a mesh. Thus, the SPDE approach can be employed to model the intensity surface and the same nodes reused in evaluation of the Poisson process likelihood. The result is a substantial improvement in both computing time and accuracy of the approximation compared to gridding.

The approximation arises from a factorization of the Poisson process likelihood. For notational clarity, assume  $\log[\lambda(u)] = \Psi(u)$ . The exact log-likelihood is

$$\ell(\lambda) = C - \int \lambda(u) du + \sum_{i=1}^n \log[\lambda(x_i)]$$

where  $C$  is a normalizing constant. The log-intensity rewritten using the GMRF representation from the SPDE approach,

$$\log [\lambda(u)] \approx \sum_{j=1}^m \psi_j \phi_j(u).$$

This defines a numerical integration scheme at nodes  $s_i$  with weights  $\alpha_i$ , where the weight is the observed area in  $\text{dual}(s_i)$ , and yields the approximation,

$$\begin{aligned} \ell(\lambda) &\approx C - \sum_{i=1}^m \alpha_i \exp \left[ \sum_{j=1}^m \psi_j \phi_j(s_i) \right] + \sum_{i=1}^n \sum_{j=1}^m \psi_j \phi_j(x_i) \\ &= C - \boldsymbol{\alpha}' \exp [\mathbf{A}\boldsymbol{\psi}] + \mathbf{y}' \mathbf{A}\boldsymbol{\psi}. \end{aligned}$$

We have introduced some simplifying notation. The weight vector

$$\boldsymbol{\alpha} = (\alpha_1, \dots, \alpha_m, 0, \dots, 0)',$$

contains the weight for each node and then  $n$  zeros corresponding to the events.  $\mathbf{y}$  is a pseudodata response vector with entries  $y_i = 0$  corresponding to the nodes  $s_i$  and  $y_{m+i} = 1$  to the events  $x_i$ .  $\mathbf{A}$  is an  $m+n$  by  $m$  matrix where the first  $m$  rows are the barycentric coordinates of each node and the final  $n$  rows are the barycentric coordinates of each event.

The rewritten log-likelihood is equivalent to the log-likelihood of independent Poisson random variables with means  $\alpha_i \eta_i$  and response vector  $\mathbf{y}$ . The  $\alpha_i$  weights play the role of an offset.  $\eta_i$  is the intensity at the location of  $y_i$ , which is being modeled by the GMRF. Thus, the SPDE approach, which can be easily implemented in R-INLA, can be combined hierarchically with a Poisson GLMM to rapidly fit a LGCP model. There is no need to compute grid counts, only to define dummy points at the mesh nodes and construct a pseudodata vector  $\mathbf{y}$ .

### 2.3. Variable Sampling Effort

There has long been a gap between point process modeling theory and practice, where point process models are only fit to data from completely-observed domains under the assumption that every event was detected perfectly. In practice, this is not the case as it may be impossible or impractical to census the entire region of interest. For example, line-transect surveys routinely generate point pattern data but are analyzed after aggregation rather than using a point process model. Another issue is that of false negatives, in other words events which exist but are not detected during the survey. False negatives are an accepted part of species abundance and occupancy surveys, where the species of interest may be camouflaged or hidden in thick cover [9, 21, 23].

The idea of the incompletely-observed domain has been around for some time. Brix and Möller (2001) fit an LGCP model to weed data observed in rectangular frames and used a Metropolis-adjusted Langevin algorithm to predict the intensity outside of the observed frames [8]. Chakraborty et. al (2011) discuss nonhomogeneous Poisson process modeling as a richer alternative to ecological presence/absence models and describe their data as “degraded” in the sense that sampling bias prevented the entire region from being fully observed; they fit their model by aggregating the point pattern

to counts in grid cells and using MCMC [10]. Gabriel et. al. (2016, 2017) derived a relationship between the Kriging predictor and the LGCP to predict the LGCP intensity across an unobserved subset of the region of interest [15, 16].

With INLA, the SPDE approach, and the “off grid” approximation facilitating the routine fitting of LGCP models, there is now renewed interest in accounting for variable sampling effort in spatial point process models [30, 33].

Sampling effort is accounted for using the theory of thinned point processes. Thinning refers to the events of one point process being kept or discarded probabilistically. Let  $\lambda(u)$  be the intensity of the parent process, and let an event  $x = u$  (if it exists) be observed with probability  $p(u)$ . The observed point process is a thinned point process with intensity

$$\lambda_p(u) = p(u)\lambda(u),$$

and if the parent process is a Poisson process then the observed process is also a Poisson process [26].

We seek to make posterior inferences about the parent intensity,  $\lambda(u)$ . If  $p(u)$  is known, its value at each node is used to adjust the SPDE integration weights. Most usefully, if it is known that  $p(s) = 0$  at certain nodes  $s$  because they were outside the surveyed domain, the weights become zero so those nodes do not contribute to the integral. More generally, when a known subdomain is surveyed,  $p(u)$  is an indicator function for  $u$  being in the surveyed region. When  $p(u)$  is known, the integration weight for node  $s_i$  is multiplied by

$$\int_{\text{dual}(s_i)} p(u) du$$

which, for indicator functions, is simply the proportion of the dual region that is inside the surveyed region.

If  $p(u)$  is unknown, it can be modeled. Taking the logarithm of the thinned intensity and substituting in the basis function representation, we have the log-linear model

$$\log [\lambda_p(u)] = \log [p(u)] + \sum_{j=1}^m \psi_j \phi_j(u).$$

Thus, any log-linear model for  $p(u)$  that can be fit by INLA and the SPDE approach can be incorporated into the LGCP model. This provides a convenient way to estimate the detection function from distance sampling data; the model for  $\log(p(u))$  includes the distance to the nearest transect as a covariate. For example, Yuan et. al (2017) fit such a model to data from a line-transect survey using a spline model to account for the unknown detection function [33].

### 3. Applications

#### 3.1. *Beilschmiedia Pendula Lauraceae* Dataset

For an example analysis of real-world data, we consider the locations of  $n = 3605$  *Beilschmiedia pendula Lauraceae* trees in a 1000 meter by 500 meter plot in a tropical rainforest on Barro Colorado Island, Panama [24]. This dataset has appeared as an

example in several articles, including the original INLA paper where the events were aggregated to grid cell counts. We present an analysis that does not use aggregation.

The data are available as the `bei` dataset in the `spatstat` R package [4]. The point pattern is accompanied by elevation and gradient covariates measured on a square lattice with 5 m spacing. The point pattern exhibits inhomogeneity which appears to be associated with elevation and the elevation gradient (Figure 4).

### 3.1.1. Model Specification

We use the log-Gaussian Cox process model with intensity

$$\log[\lambda(u)] = \beta_0 + \beta_1 z_1(u) + \beta_2 z_2(u) + \mathbf{e}(u)$$

where  $z_1(u)$  is the elevation at  $u$ ,  $z_2(u)$  is the magnitude of the elevation gradient at  $u$ , and  $\mathbf{e}(u)$  is a zero-mean stationary and isotropic Gaussian process with Matérn covariance and fixed  $\alpha = 2$ . We parameterize the GP in terms of the standard deviation  $\sigma$  and effective range  $\rho$ . To connect this with the notation from 1.2,  $\boldsymbol{\theta} = (\sigma, \rho)'$  and  $\boldsymbol{\xi} = (\beta_0, \beta_1, \beta_2, \mathbf{e}(s_1), \dots, \mathbf{e}(s_m))'$ .

The prior distributions are set as follows.  $\beta_0$ ,  $\beta_1$ , and  $\beta_2$  are independent  $N(0, \infty)$ . For the Matérn covariance parameters, R-INLA provides a penalized complexity (PC) prior defined in terms of the standard deviation  $\sigma$  and the effective range  $\rho$  [14, 31]. The PC prior is intended to provide an intuitive way to define informative priors and is specified by defining a tail probability for each parameter. INLA actually uses these inputs to set an exponential prior on the precision  $\tau = 1/\sigma^2$  and a Weibull prior on the scale  $\kappa = \sqrt{8\nu}/\rho$ , but all of the software output is provided in terms of  $\sigma$  and  $\rho$ . We set  $\Pr(\sigma > 2) = 0.1$  to be relatively uninformative for the SD of a log-scale random effect, and  $\Pr(\rho < 5) = 0.1$  similar to the prior used by Möller and Waagepetersen [24].

### 3.1.2. Fitting in R-INLA

We fit the model in R using the INLA package and its implementation of the SPDE approach. Some manual preprocessing was needed to employ the Poisson factorization. Our R code can be found in the supplementary materials. This section provides a conceptual explanation of the model-fitting process.

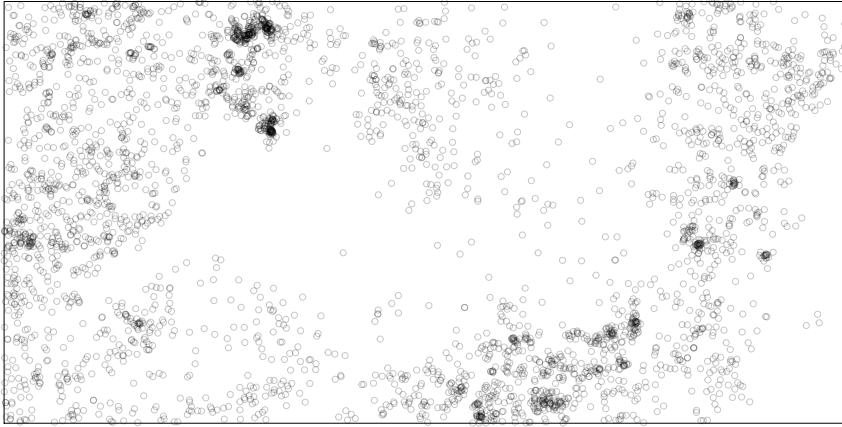
The first task is to construct a mesh for the piecewise linear approximations. A 25 meter resolution appears adequate to accurately represent the covariate surfaces. We used tools in the INLA package to create a Delaunay triangulation with a maximum edge length of 25 m. The resulting mesh has  $m = 2145$  nodes  $s_1, \dots, s_{2145}$  and 4096 triangles (Figure 5). We used linear interpolation to approximate the covariates  $z_1(s_i)$  and  $z_2(s_i)$  at each node. After creating the mesh, we specify the priors for the covariance parameters and INLA can initialize an object to represent the covariance structure on the mesh.

The next step is to define the pseudodata, find the barycentric coordinate matrix  $\mathbf{A}$ , and calculate the numerical integration weights. The pseudodata vector is

$$\mathbf{y} = (0, \dots, 0, 1, \dots, 1)'$$

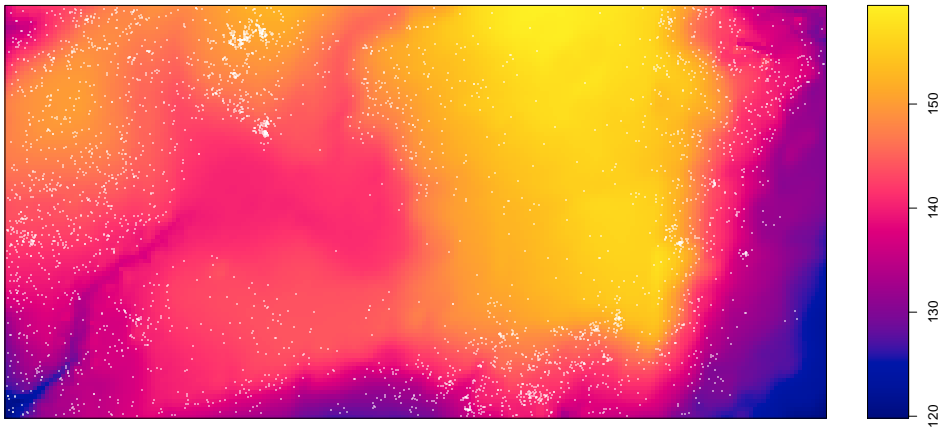
consisting of 2145 zeros corresponding to the mesh nodes and 3604 ones representing the events. The first 2145 rows of  $\mathbf{A}$  are an identity matrix; the remaining rows are the barycentric coordinates of the events, which R-INLA calculates for us. The weight

*Beilschmiedia pendula* Lauraceae Locations



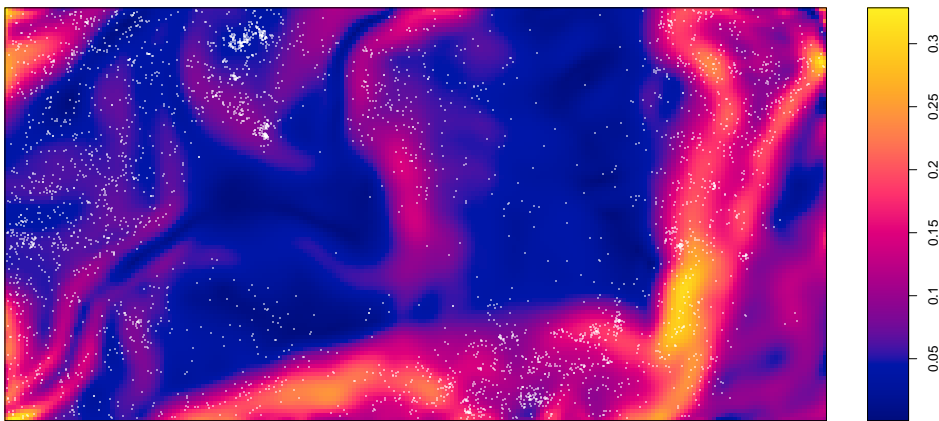
(a) Locations of trees (events).

Elevation



(b) Elevation in meters, with events overlaid.

Gradient



(c) Magnitude of the elevation gradient, with events overlaid.

**Figure 4.** Plots of the event and covariate data for the real-world data analysis. The study region is 1000 m by 500 m.

Mesh Over Bei Data

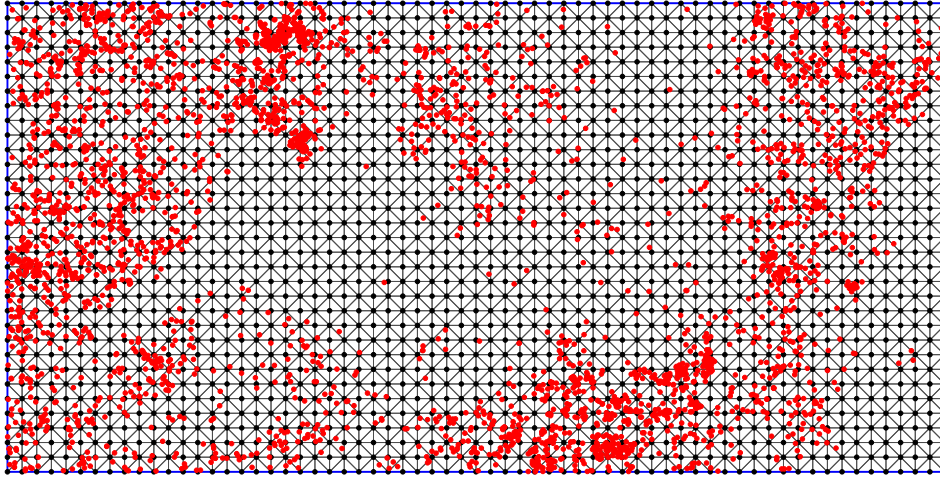


**Figure 5.** Triangular mesh with pseudodata overlaid for the real-world data analysis. Black dots represent pseudodata with values of 0 at the mesh nodes. Red dots represent pseudodata with values of 1 at the events.

vector is

$$\boldsymbol{\alpha} = (\alpha_1, \dots, \alpha_{2145}, 0, \dots, 0)'.$$

The alphas equal one-third of the total area of all triangles of which each node is a vertex, calculated by the `INLA` package. The zeros correspond to the 3604 events, which do not contribute to the numerical integration.

The final bit of setup is to combine the pseudodata, covariates at the nodes, and a vector of node indices into a data list for the `inla()` function. This function is then called with arguments specifying a formula for the linear predictor, a Poisson family model (which defaults to a log link), the data list, the  $\mathbf{A}$  matrix, the priors for the coefficients, and the  $\boldsymbol{\alpha}$  vector as the exposure parameter. This function delivers the posterior marginal distribution of each parameter, latent variable, and any requested linear combinations of those. The `inla()` function takes about 90 seconds to fit the model on a midrange laptop.

### 3.1.3. Results

The posterior marginals provide evidence that both higher elevation and larger gradient are associated with higher intensity. The elevation coefficient  $\beta_1$  has a posterior mean of 0.0328 with a central 95% interval of (0.0112, 0.0547), and the gradient coefficient  $\beta_2$  has posterior mean 4.44 with 95% interval (2.42, 6.46). The posterior mean of the intercept  $\beta_0$  is  $-10.9$  with 95% interval of  $(-14.2, -7.63)$ . Mapped across space, the posterior mean of the fixed effect component of the linear predictor,

$$E(\beta_0|\mathbf{x}) + E(\beta_1|\mathbf{x})z_1(u) + E(\beta_2|\mathbf{x})z_2(u),$$

appears as an average of the elevation and gradient surfaces (Figure 6, top).

The fixed effects do not explain all of the heterogeneity of the point pattern; some spatial structure remains to be described by the posterior predicted GP (Figure 6, bot-

tom). The prediction surface shows a large region of low values in the center where there are nearly no events, and hotspots where many events are clumped together. The GP standard deviation  $\sigma$  has posterior mean 1.30 and 95% central interval (1.05, 1.63), while the range parameter  $\rho$  has a posterior mean of 176 with a 95% interval of (137, 229).

#### 3.1.4. Model Checking

This section provides a brief and simple residual analysis to illustrate that there are no glaring issues with the model fit. Literature on residual analysis for spatial point process models is quite rich and not specific to INLA; for a more general discussion see Baddeley et. al. (2005) [5].

We calculated the Pearson residuals,

$$\frac{\text{Observed count} - \text{Expected count}}{\sqrt{\text{Expected count}}},$$

on a 40 by 20 lattice of grid cells. We used functions from R-INLA to transform predictions from the log-scale to the natural scale and calculate the posterior mean intensity at the center of each grid cell (Figure 7, top). The expected counts were approximated by the posterior mean intensity times the area of the grid cell. The bottom panel of Figure 7 shows the Pearson residuals mapped across space.

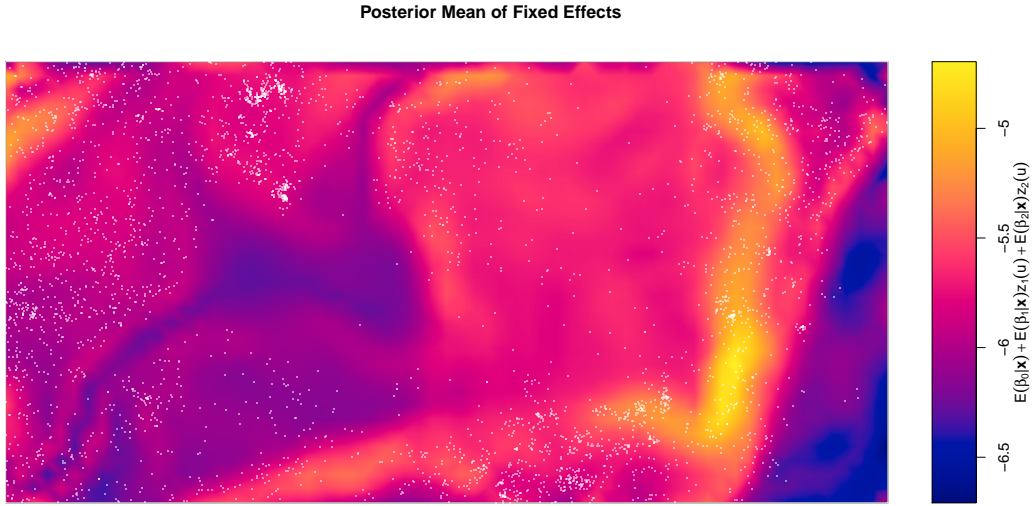
The residuals have small magnitude in the central region and on the eastern edge where there are no observed events and low mean posterior intensity. This is not surprising because it is not possible to see much variation in counts in that region. There are a few large-magnitude positive residuals (about 4) suggesting there is some clustering not described by the model. Elsewhere, the residuals appear random with no obvious spatial patterns. We repeated the residual analysis with several grid cell sizes and saw the same characteristics each time.

### 3.2. Transect Sampling Example

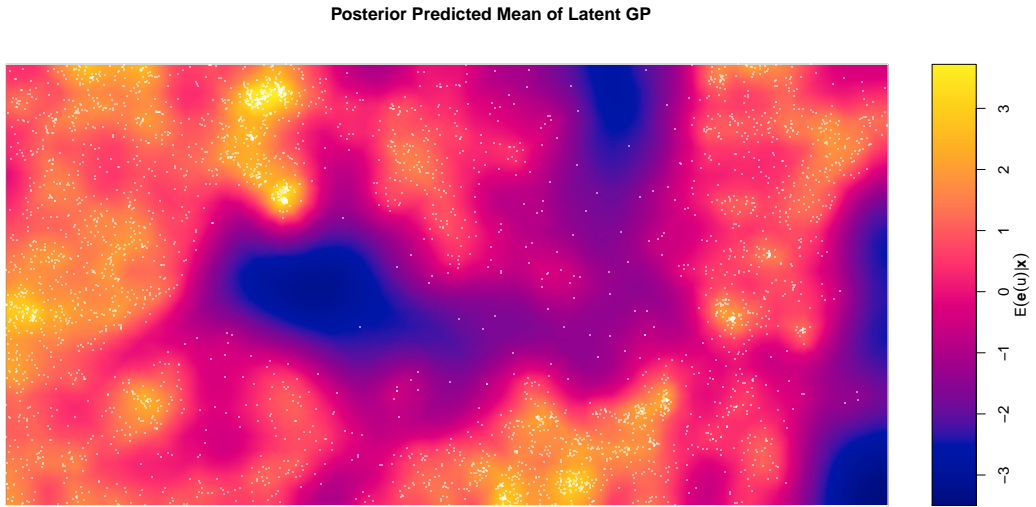
In this section, we illustrate the analysis of incompletely-observed point pattern data using the *Beilschmiedia pendula* Lauraceae and a simulated transect sampling scheme. The example uses a survey scheme where all events in a subset of the study region are recorded. This type of variable sampling effort requires more programming effort than distance sampling, and the difference is worth explaining. We also provide R code for a distance sampling example in the supplementary materials, but the preprocessing and model-fitting procedure for distance sampling data is not much more complicated than for the fully-observed case.

Suppose part of the study requires every observed tree to be visited so time-consuming measurements can be made on each. For practical reasons, the researchers decide to take a systematic sample of transects and limit data collection to events within 5 m of a transect. Sections of the site farther than 5 m from a transect are unobserved, meaning events in those regions cannot be observed and nothing is known about the number of events or their locations. We assume the elevation and gradient data were available from another source so that the full covariate data can be used to predict the intensity in the unobserved parts of the site.

We simulate this by choosing a random starting point and defining transects running north-south spaced 50 m apart. All events within 5 m of a transect are saved; all other



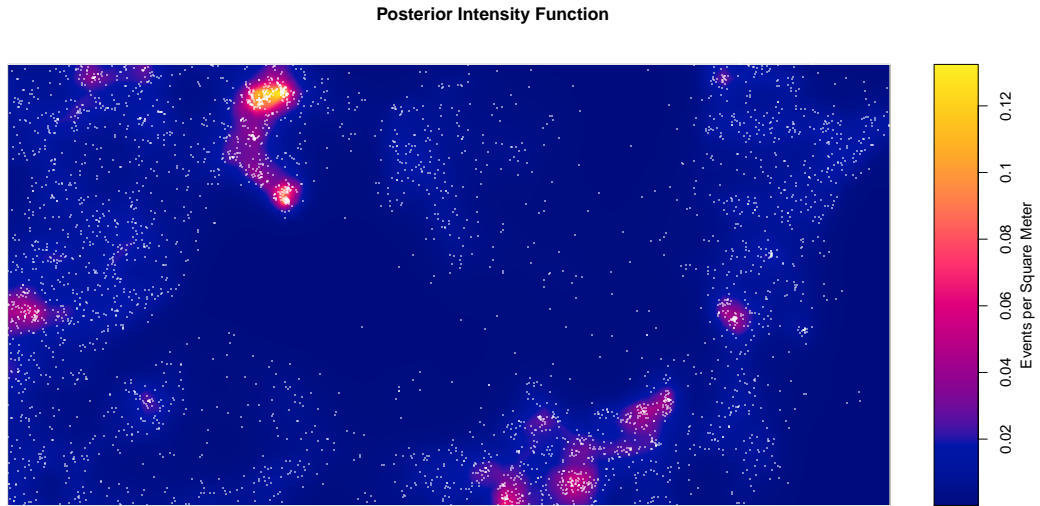
(a) Posterior mean surface for the fixed effects.



(b) Posterior mean of the GP prediction surface.

**Figure 6.** Posterior mean surfaces of the fixed effects component and the spatial GP from the real-world data analysis.





(a) Posterior intensity surface in events per square meter, calculated using the piecewise linear approximate covariate surfaces and the posterior means of the intercept, coefficients, and GP.



(b) Pearson residuals calculated on a grid.

**Figure 7.** Posterior mean intensity function and Pearson residuals calculated using the posterior mean intensity from the real-world data analysis.

events are discarded. The result is  $n = 710$  events observed in 20 rectangles sized 500 m by 10 m (Figure 8).

### 3.2.1. Model Specification

We use the same model as fit to the full data, a log-Gaussian Cox process model with intensity

$$\log [\lambda(u)] = \beta_0 + \beta_1 z_1(u) + \beta_2 z_2(u) + \mathbf{e}(u).$$

As before,  $z_1(u)$  is the elevation at  $u$ ,  $z_2(u)$  is the magnitude of the elevation gradient at  $u$ , and  $\mathbf{e}(u)$  is a zero-mean Gaussian process with Matérn covariance and  $\alpha = 2$ . The prior distributions are again  $\beta_0$ ,  $\beta_1$ , and  $\beta_2$  independent  $N(0, \infty)$ ,  $\Pr(\sigma > 2) = 0.1$ , and  $\Pr(\rho < 5) = 0.1$ .

### 3.2.2. Fitting in R-INLA

The procedure for fitting the LGCP model to variable sampling effort data is the same as for fully-observed data except that the weight vector  $\boldsymbol{\alpha}$  is different. Our code is available in the supplementary materials.

The mesh (Figure 9) is the same as used with the fully-observed point pattern, with  $m = 2145$  nodes. We interpolated the covariates at the nodes and had INLA can initialize the covariance structure as before. The pseudodata vector changes dimension, becoming

$$\mathbf{y} = (0, \dots, 0, 1, \dots, 1)'$$

with 2145 zeros corresponding to the mesh nodes and 710 ones for the observed events.

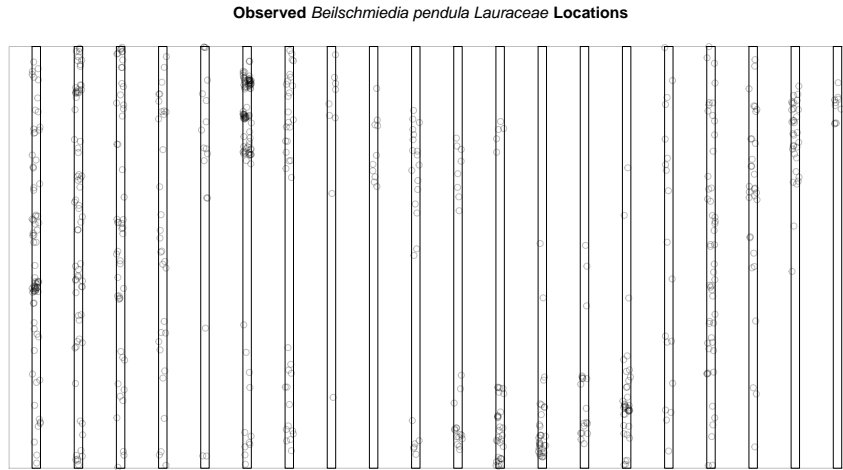
The computation of the weight vector is more involved. The notation is again

$$\boldsymbol{\alpha} = (\alpha_1, \dots, \alpha_{2145}, 0, \dots, 0)',$$

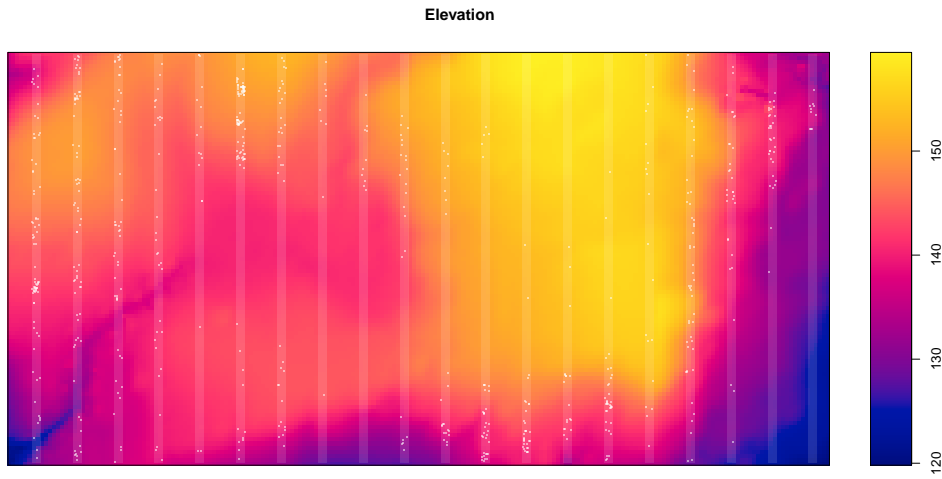
now with 710 zeros representing the observed events. The alphas equal the observed area represented by each node. We used tools from **spatstat** to calculate these areas. First, we created an **owin** object defining the observed region along the transects. Then, we created a list of **owin** objects with each representing one triangle of the mesh. Next, we intersected the observed region with each triangle to partition the observed region into many small shards, each contained within a single triangle (Figure 10). Then we calculated the area of each shard. These areas are each associated with a triangle, but the need to be allocated to the nodes at the vertices of the triangle. To do this, we found the centroid of each shard and allocated the area proportional to the barycentric coordinates of the centroid. This way, the area of each shard is distributed to the three nodes which define the triangle, and the closest node gets the most weight while the farthest node get the least weight. Finally, the alpha value for each node is computed by summing the weights contributed by each shard to that node.

*Is there a better (or more formal) term than “shard”? It has an intuitive meaning to me, but it feels weird to create nonstandard terminology for use in exactly one paragraph. —Kenny*

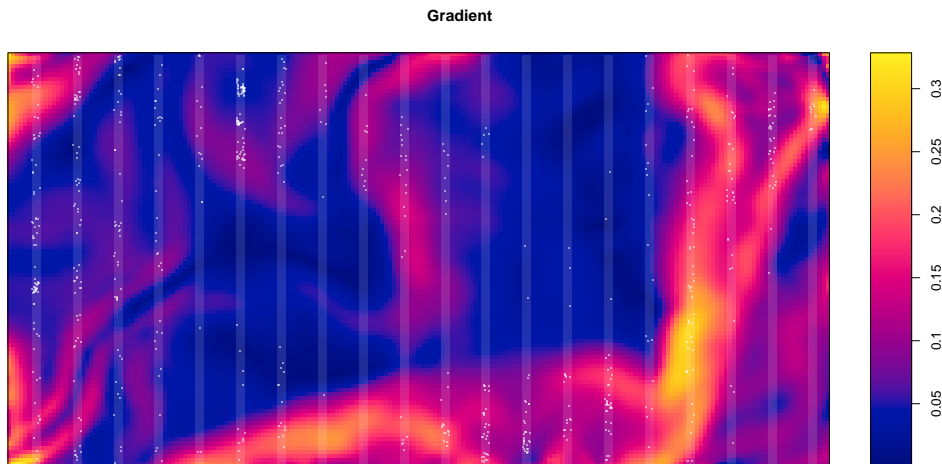
Finally, the pseudodata, covariates, and a node index are combined into a data list and the **inla()** function is called to fit the model. The model takes about 65 seconds to fit on our laptop computer.



(a) Locations of observed trees (events).



(b) Elevation in meters, with observed region and events overlaid.



(c) Magnitude of the elevation gradient, with observed region and events overlaid.

**Figure 8.** Plots of the event and covariate data for the simulated transect survey. The study region is 1000 m by 500 m.

Mesh Over Bei Data

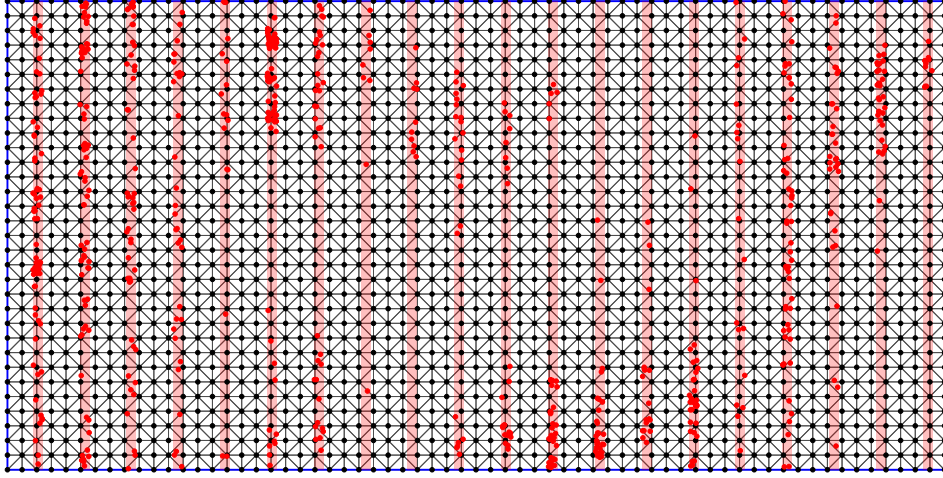


**Figure 9.** Triangular mesh with observed region and events overlaid for the simulated transect data analysis. Black dots represent pseudodata with values of 0 at the mesh nodes. Red dots represent pseudodata with values of 1 at the observed events.

Partition of the Observed Region

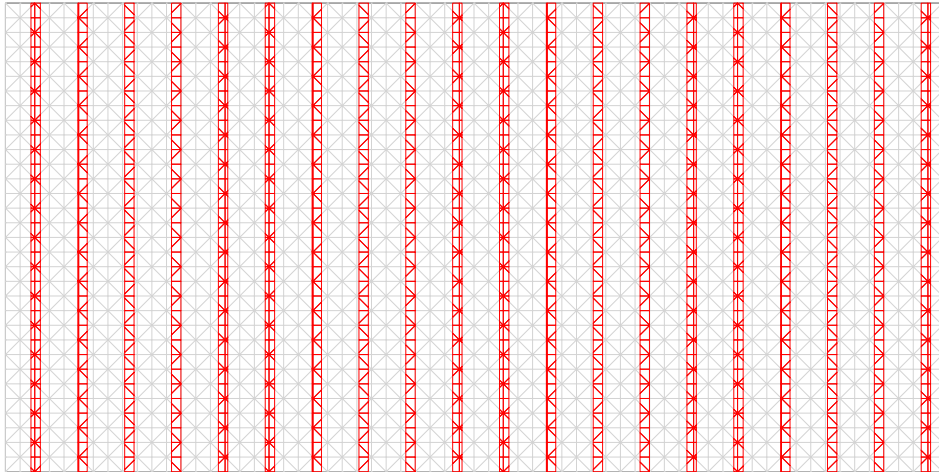


**Figure 10.** Partition of the observed region created by intersection with each mesh triangle.

### 3.2.3. Results

The fixed effect posterior marginals give evidence of relationships between the intensity and both elevation and gradient. The elevation coefficient  $\beta_1$  has a posterior mean of 0.0444 and a central 95% posterior interval of (0.00686, 0.0836). The gradient coefficient  $\beta_2$  has a posterior mean of 6.21 and a 95% interval of (3.24, 9.20). The intercept  $\beta_0$  has posterior mean  $-12.7$  and 95% interval  $(-18.6, -7.10)$ . The posterior mean of the fixed effect component of the linear predictor again appears as an average of the elevation and gradient surfaces (Figure 11, top), very similar to the previous figure.

As before, there is some additional spatial structure described by the GP (Figure 11, bottom). The prediction surface has low values in the center and north where no events were observed, hotspots where events are concentrated along the transects, and smooth transitions across the unsurveyed regions between transects. The standard deviation  $\sigma$  has a posterior mean of 1.27 with a central 95% posterior interval of (0.956, 1.70). The range  $\rho$  has a posterior mean of 232 and 95% interval of (161, 340).

### 3.2.4. Model Checking

To assess the model fit, we computed Pearson residuals on a 40 by 20 lattice of grid cells. The expected counts were approximated by the multiplying the posterior mean intensity (Figure 12, top) at the center of each grid cell times the observed area within the cell. Cells with no observed area have undefined residuals and appear white in the plot (Figure 12, bottom).

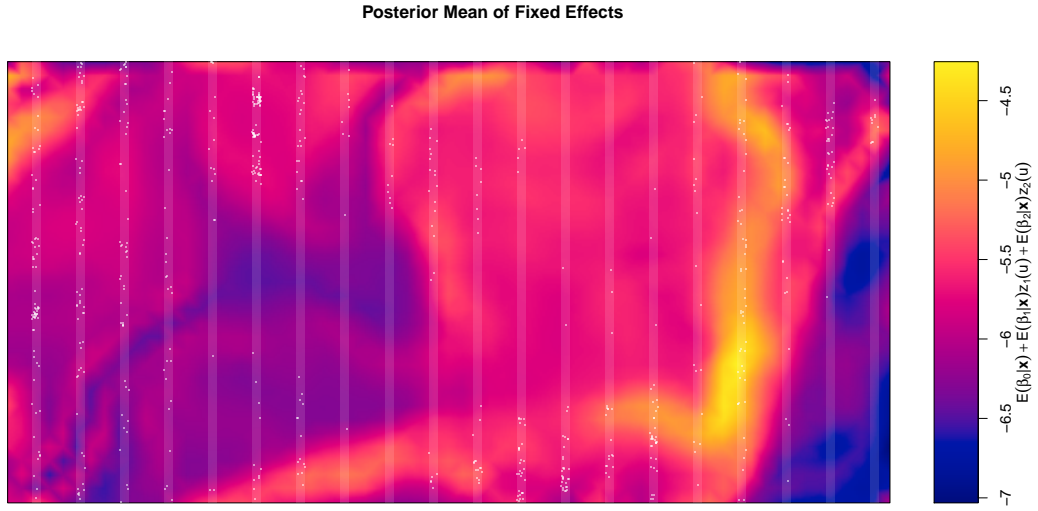
The residuals have low magnitude in the large regions with no observed events and low posterior intensity. There are more large positive residuals than large-magnitude negative residuals, including in several places where events appear to form small clusters. Otherwise, the residuals appear random with no obvious spatial patterns.

## 4. Conclusion and Discussion

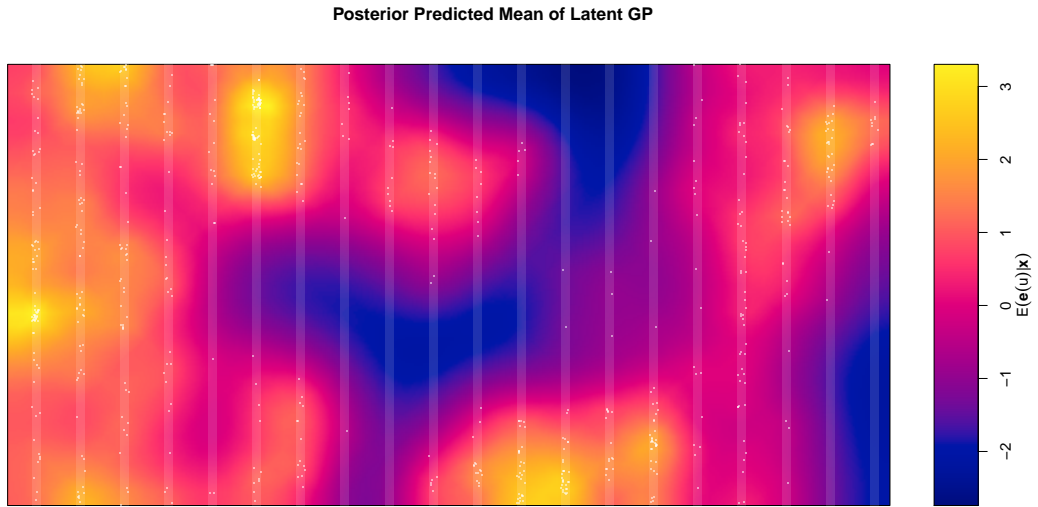
The SPDE approach, Poisson factorization, INLA, and the R-INLA software make it practical to fit Bayesian spatial LGCP models to real data. It is possible to make useful maps of spatial predictions with only the pointwise posterior marginals.

The example analyses in this article, using a full real-world dataset and simulated variable sampling effort applied to the same dataset, show that these tools can facilitate accurate inference from data collected through sampling. Both models yielded similar posterior marginal distributions for the coefficients and the standard deviation. The posterior intervals from the model fit to the sampled dataset were wider, as expected due to the smaller area surveyed, but the intervals from both models still have quite a bit of overlap. For the linear predictor, the posterior mean surfaces from both models look very similar when mapped across space (Figures 6 and 11, top panels).

Our example models differ in the posterior distributions of the predicted GP and the range. The GP prediction surfaces have the same large-scale structure, but the surface from the model fit to the sampled data (Figure 11) is noticeably smoother than the surface inferred from the complete data (Figure 6 for sampled, bottom panels). This is related to the range; the posterior interval for the range when using the sampled data (161 to 340) is much wider and shifted to the right compared the interval when using the complete data (137 to 229). The reason for this is that the LGCP model simply cannot predict detail in regions far from the observed sections of the site, and there are no data in those unobserved regions to constrain possible values of the range. Indeed,

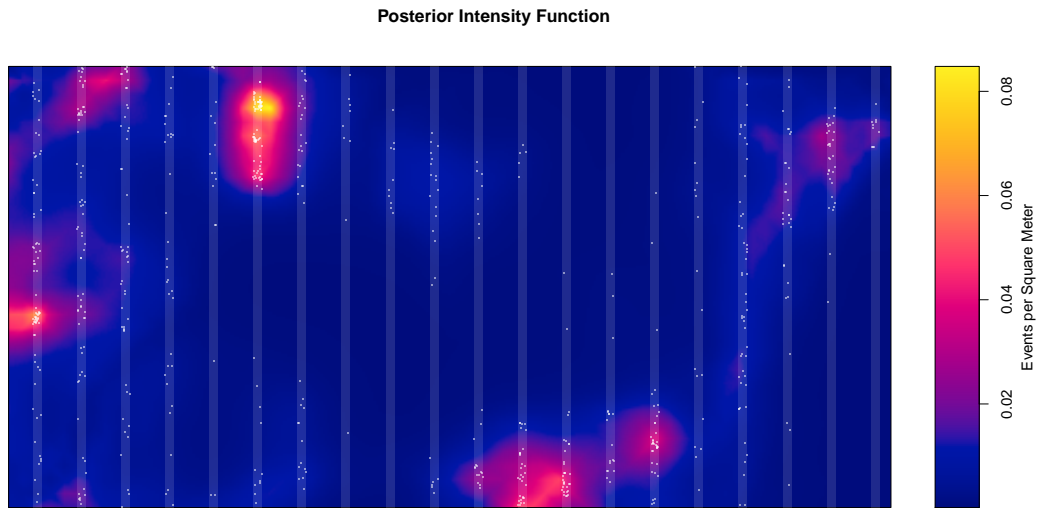


(a) Posterior mean surface for the fixed effects.



(b) Posterior mean of prediction surface.

**Figure 11.** Posterior mean surfaces of the fixed effects component and the spatial GP from the simulated transect data analysis.



(a) Posterior intensity surface in events per square meter, calculated using the piecewise linear approximate covariate surfaces and the posterior means of the intercept, coefficients, and GP.



(b) Pearson residuals calculated on a grid.

**Figure 12.** Posterior mean intensity function and Pearson residuals calculated using the posterior mean intensity from the simulated transect data analysis.

Simpson et. al. (2016) discussed this and suggested coarsening the mesh in unsurveyed regions where extra detail is not needed [30].

Construction of the mesh requires consideration of both the latent GP and any covariates. The mesh used in the examples was developed to accurately represent details in the covariate surfaces, and is finer than needed to describe the GP. These examples are not particularly complex, but if computation needed to be further simplified, the mesh could be adaptively coarsened or refined depending on the local complexity of the covariates.

We have illustrated that, using these tools, spatial mapping based on Bayesian LGCP models is now practical with useful accuracy in short amount of time. This includes when the point pattern is incompletely observed. We look forward to wider application of spatial LGCP models and future advancements in sampling for spatial point process models.

## References

- [1] F.E. Bachl, F. Lindgren, D.L. Borchers, and J.B. Illian, *inlabru: an R package for bayesian spatial modelling from ecological survey data*, Methods in Ecology and Evolution 10 (2019), pp. 760–766.
- [2] A. Baddeley, J.F. Coeurjolly, E. Rubak, and R. Waagepetersen, *Logistic regression for spatial gibbs point processes*, Biometrika 101 (2014), pp. 377–392.
- [3] A. Baddeley and R. Turner, *Practical maximum pseudolikelihood for spatial point patterns*, Australian & New Zealand Journal of Statistics 42 (2000), pp. 283–322.
- [4] A. Baddeley and R. Turner, *Spatstat: An R package for analyzing spatial point patterns*, Journal of Statistical Software 12 (2005), pp. 1–42.
- [5] A. Baddeley, R. Turner, J. Møller, and M. Hazelton, *Residual analysis for spatial point processes*, Journal of the Royal Statistical Society: Series B (Statistical Methodology) 67 (2005), pp. 617–666.
- [6] M. Berman and T.R. Turner, *Approximating point process likelihoods with glim*, Applied Statistics (1992), pp. 31–38.
- [7] M. Blangiardo and M. Cameletti, *Spatial and Spatio-temporal Bayesian Models with R-INLA*, Wiley, 2015.
- [8] A. Brix and J. Møller, *Space-time multi type log gaussian cox processes with a view to modelling weeds*, Scandinavian Journal of Statistics 28 (2001), pp. 471–488.
- [9] S. Buckland, E. Rexstad, T. Marques, and C. Oedekoven, *Distance Sampling: Methods and Applications*, Springer, 2015.
- [10] A. Chakraborty, A.E. Gelfand, A.M. Wilson, A.M. Latimer, and J.A. Silander, *Point pattern modelling for degraded presence-only data over large regions*, Journal of the Royal Statistical Society: Series C (Applied Statistics) 60 (2011), pp. 757–776.
- [11] D.R. Cox, *Some statistical methods connected with series of events*, Journal of the Royal Statistical Society: Series B (Methodological) 17 (1955), pp. 129–157.
- [12] N. Cressie, *Statistics for Spatial Data*, Wiley, 1993.
- [13] P. Diggle, *Statistical Analysis of Spatial and Spatio-Temporal Point Patterns*, 3rd ed., CRC Press, 2013.
- [14] G.A. Fuglstad, D. Simpson, F. Lindgren, and H. Rue, *Constructing priors that penalize the complexity of gaussian random fields*, Journal of the American Statistical Association 114 (2019), pp. 445–452.
- [15] E. Gabriel, F. Bonneau, P. Monestiez, and J. Chadoeuf, *Adapted kriging to predict the intensity of partially observed point process data*, Spatial Statistics 18 (2016), pp. 54–71.
- [16] E. Gabriel, J. Coville, and J. Chadoeuf, *Estimating the intensity function of spatial point processes outside the observation window*, Spatial Statistics 22 (2017), pp. 225–239.
- [17] J.B. Illian, S.H. Sørbye, and H. Rue, *A toolbox for fitting complex spatial point process*



- models using integrated nested laplace approximation (INLA)*, The Annals of Applied Statistics (2012), pp. 1499–1530.
- [18] G. Konstantinoudis, D. Schuhmacher, H. Rue, and B.D. Spycher, *Discrete versus continuous domain models for disease mapping*, Spatial and Spatio-temporal Epidemiology 32 (2020), p. 100319.
  - [19] F. Lindgren and H. Rue, *Bayesian spatial modelling with R-INLA*, Journal of Statistical Software 63 (2015), pp. 1–25.
  - [20] F. Lindgren, H. Rue, and J. Lindström, *An explicit link between gaussian fields and gaussian markov random fields: the stochastic partial differential equation approach*, Journal of the Royal Statistical Society: Series B (Statistical Methodology) 73 (2011), pp. 423–498.
  - [21] W. Link and R. Barker, *Bayesian Inference: With Ecological Applications*, Elsevier, 2009.
  - [22] L. Lombardo, T. Opitz, and R. Huser, *Point process-based modeling of multiple debris flow landslides using inla: an application to the 2009 messina disaster*, Stochastic environmental research and risk assessment 32 (2018), pp. 2179–2198.
  - [23] D. MacKenzie, J. Nichols, J. Royle, K. Pollock, L. Bailey, and J. Hines, *Occupancy Estimation and Modeling: Inferring Patterns and Dynamics of Species Occurrence*, Elsevier, 2017.
  - [24] J. Møller and R. Waagepetersen, *Modern spatial point process modelling and inference*, Scandinavian Journal of Statistics 34 (2007), pp. 643–711.
  - [25] J. Møller, A.R. Syversveen, and R.P. Waagepetersen, *Log gaussian cox processes*, Scandinavian journal of statistics 25 (1998), pp. 451–482.
  - [26] J. Møller and R.P. Waagepetersen, *Statistical Inference and Simulation for Spatial Point Processes*, CRC Press, 2003.
  - [27] J. Neyman and E.L. Scott, *Statistical approach to problems of cosmology*, Journal of the Royal Statistical Society. Series B (Methodological) (1958), pp. 1–43.
  - [28] H. Rue, S. Martino, and N. Chopin, *Approximate bayesian inference for latent gaussian models by using integrated nested laplace approximations*, Journal of the royal statistical society: Series b (statistical methodology) 71 (2009), pp. 319–392.
  - [29] P. Samartsidis, C.R. Eickhoff, S.B. Eickhoff, T.D. Wager, L.F. Barrett, S. Atzil, T.D. Johnson, and T.E. Nichols, *Bayesian log-gaussian cox process regression: applications to meta-analysis of neuroimaging working memory studies*, Journal of the Royal Statistical Society: Series C (Applied Statistics) 68 (2019), pp. 217–234.
  - [30] D. Simpson, J.B. Illian, F. Lindgren, S.H. Sørbye, and H. Rue, *Going off grid: Computationally efficient inference for log-gaussian cox processes*, Biometrika 103 (2016), pp. 49–70.
  - [31] D. Simpson, H. Rue, A. Riebler, T.G. Martins, S.H. Sørbye, *et al.*, *Penalising model component complexity: A principled, practical approach to constructing priors*, Statistical science 32 (2017), pp. 1–28.
  - [32] M. Taddy, *Autoregressive mixture models for dynamic spatial poisson processes: Application to tracking intensity of violent crime*, Journal of the American Statistical Association 105 (2010), pp. 1403–1417.
  - [33] Y. Yuan, F.E. Bachl, F. Lindgren, D.L. Borchers, J.B. Illian, S.T. Buckland, H. Rue, T. Gerrodette, *et al.*, *Point process models for spatio-temporal distance sampling data from a large-scale survey of blue whales*, The Annals of Applied Statistics 11 (2017), pp. 2270–2297.